Published in final edited form as:
IEEE Rev Biomed Eng. 2014 ; 7: 87–96. doi:10.1109/RBME.2013.2297206.

Magnetic Resonance Based Electrical Properties Tomography: A Review

Xiaotong Zhang,
Department of Biomedical Engineering, University of Minnesota, Minneapolis, MN 55455, USA

Jiaen Liu, and
Department of Biomedical Engineering, University of Minnesota, Minneapolis, MN 55455, USA

Bin He [Fellow IEEE]
Department of Biomedical Engineering and Institute for Engineering in Medicine, University of Minnesota, Minneapolis, MN 55455, USA

Bin He: binhe@umn.edu

Abstract

Frequency-dependent electrical properties (EPs; conductivity and permittivity) of biological tissues provide important diagnostic information (e.g. tumor characterization), and also play an important role in quantifying radiofrequency (RF) coil induced Specific Absorption Rate (SAR) which is a major safety concern in high- and ultrahigh-field Magnetic Resonance Imaging (MRI) applications. Cross-sectional imaging of EPs has been pursued for decades. Recently introduced Electrical Properties Tomography (EPT) approaches utilize the measurable RF magnetic field induced by the RF coil in an MRI system to quantitatively reconstruct the EP distribution *in vivo* and non-invasively with a spatial resolution of a few millimeters or less. This paper reviews the Electrical Properties Tomography approach from its basic theory in electromagnetism to the state of the art research outcomes. Emphasizing on the imaging reconstruction methods rather than experimentation techniques, we review the developed imaging algorithms, validation results in physical phantoms and biological tissues, as well as their applications in *in vivo* tumor detection and subject-specific SAR prediction. Challenges for future research are also discussed.

Index Terms

Electrical Properties Tomography; EPT; Bioimepdance; Magnetic Resonance Imaging; B_1-mapping; SAR

I. INTRODUCTION

The electrical properties (EPs), which consist of the conductivity and the permittivity, largely vary as a function of the relative intracellular and extracellular fluid volumes and

Correspondence to: Bin He, binhe@umn.edu.

ionic concentrations, and the cellular membrane extent in the tissue, respectively [1]–[3]. EPs values also vary as a function of the frequency of applied electromagnetic (EM) wave. It was reported that malignant tissues differ from normal tissues (brain, breast, skin, prostate, liver, bladder etc.) in EPs, generally attributing to the different water content in neoplastic tissue due to the variation of protein hydration and vascularization, as well as to the membrane permeability, amount of extracellular fluid, packing density and orientation of the malignant cells [4]–[7]. Experimental results have shown that cancerous tissues have significantly higher EPs values than normal tissues over a wide electromagnetic frequency spectrum, e.g., >200% for breast cancer and >100% for bladder cancer via *ex vivo* measurement at radio and microwave frequencies [8]–[17]. At the same time, while in some cases it is impossible to discriminate the malignance from tumors with conventional Magnetic Resonance (MR) techniques, statistically significant EPs differences between cancerous and benign tissues were reported in *ex vivo* measurements, e.g. basal cell carcinoma vs. benign nevi, and prostate cancer vs. benign prostatic hyperplasia at radio frequencies [18]–[21]. These data suggest that development of an imaging modality for mapping electrical properties with a high spatial resolution and high specificity will have a significant impact on detection and diagnosis of cancer, and may thus improve substantially survival rate of cancer patients.

In the meantime, high- and ultrahigh-field (HF and UHF: 3 Tesla and above) MRI has been pursued with increasing interest and potentially wide clinical applications. The advantages of using HF or UHF MRI include the promise of improved signal-to-noise ratio (SNR), higher spatial resolution and increased sensitivity for contrast mechanisms such as the blood-oxygenation-level-dependent (BOLD) contrast [22]. However, elevated thermal effects due to tissue heating accompany with increased main magnetic field strength, posing a safety concern in HF-MRI applications [23]. Specific Absorption Rate (SAR) is directly related to RF-induced heating [24]; absence of quantification of local SAR values on a subject-specific basis yields a worst-case safety limit in current MRI RF power transmission, and, as a consequence, may compromise the underlying improved SNR and image contrast associated with high field MRI [25]. EPs distributions play a fundamental and important role in SAR calculation in HF-MRI – a reliable calculation of local SAR hot spots necessitates the knowledge of local tissue EPs values at the operating radiofrequency (RF) [24]. Therefore, real-time and subject-specific EPs imaging is highly desirable for SAR quantification and for the purpose of constraining tissue heating in pulse sequence design in HF-MRI applications.

There have been a number of research efforts attempting to non-invasively image EPs of biological tissues in the past decades. 1) Electrical Impedance Tomography (EIT) inversely reconstructs impedance images from electric potential measurement induced by current injection through surface electrodes [13], [26], [27]. Its merits include low cost, simplicity of application and high speed of data collection, while the major limitation lies in its poor spatial resolution due to a limited amount of measured data and the ill-posedness of the corresponding inverse problem involved in image reconstruction. 2) Magnetic Induction Tomography (MIT) uses the interaction of an oscillating magnetic field with conductive media, and the EPs can be reconstructed from the measurements of perturbed magnetic field

outside the object [28], [29]. However, similar to EIT, the surface measurements and ill-posedness of the inverse problem result in low spatial resolution. 3) Magnetic Resonance Electrical Impedance Tomography (MREIT), which originates from Magnetic Resonance Current Density Imaging (MRCDI) [30], [31], measures the local magnetic field induced by surface current injection, and reconstructs static cross-sectional conductivity images [32]–[35]. While MREIT provides high spatial resolution, what remains to be demonstrated includes the safety issues due to the usage of high level of current injection in order to achieve sufficient SNR, and the shielding effect due to the use of surface electrodes for current injection. 4) In Hall Effect Imaging (HEI), the sample is located in a static magnetic field with current injection through surface electrodes. The sample will emit acoustic waves which are collected around the object and processed to reconstruct images related with the conductivity of the tissues [36]. While HEI has the potential to obtain high resolution images, it remains to be demonstrated of its ability to quantitatively reconstruct conductivity distribution and to overcome the shielding effect. 5) Magneto-acoustic Tomography with Magnetic Induction (MAT-MI) exploits the Lorentz force effect due to the interaction of a magnetic field and eddy current induced by a time varying magnetic field, and emitted acoustic waves are collected by ultrasound transducers in proximity to the object surface for conductivity image reconstruction [37]–[39]. Current MAT-MI experimental studies focus on gel phantoms and tissue samples, and there have been no *in vivo* experiments reported so far.

By employing Maxwell's Equations that govern electromagnetic fields, MR based Electrical Properties Tomography (EPT) utilizes measurable RF-coil-induced magnetic fields (B_1 fields) in an MRI system to quantitatively reconstruct the local EPs of biological tissues. The concept of imaging EPs from MR signals was firstly suggested by Haacke et al. [40]: the wavelength of the RF radiation was of the order of the body size, leading to a distortion of the B_1 field inside the irradiated object; by using certain imaging algorithm, the EPs can be estimated using MRI images which reflect the disrupted RF profile. Wen [41] later pointed out that the perturbation of the RF field in high-field MRI directly related to the conductivity and permittivity distribution, which can be explained by electromagnetic wave equation. In recent years, EPT has drawn considerable attention by various research groups. Based upon B_1-mapping techniques in MRI measuring induced B_1 field distributions, various MR-EPT methods have been proposed using different coil designs (e.g. birdcage quadrature, multi-channel transceiver) and at different radio frequencies (64MHz~300MHz) of the operating static main field (1.5T~7T) [42]–[53].

Figure 1 shows the conceptual diagram of EPT approach. Differing from other noninvasive EPs imaging techniques, e.g. EIT or MREIT, EPT requires no electrode mounting, and no additional external energy is introduced into the body during an MRI scanning other than the inherent B_1 fields. Meanwhile, unlike EPs imaging technologies involving acoustic coupling, e.g. HEI and MAT-MI, applied B_1 fields could easily penetrate into most biological tissues, making EPT suitable for whole body imaging. In addition, MR-EPT is performed using a standard MRI system with regular RF coils, and its spatial resolution is determined by MRI images and the quality of the employed B_1-mapping technique.

The following sections review the recent cutting-edge development of EPT, from its basic theories in electromagnetism to the most recent research outcomes. We focus our discussions on the mathematical reconstruction methods and inverse imaging algorithms, the validation results, as well as applications in *in vivo* tumor detection and subject-specific SAR estimation.

II. MAPPING RF-COIL-INDUCED MAGNETIC FIELDS

In MRI, there are several types of magnetic fields applied to manipulate the magnetic moments of nuclei in tissues to generate MR signals. Besides the static magnetic field from the main MR magnet (B_0) which aligns nuclear spins along itself under the equilibrium state, the RF magnetic field (B_1) induced by the RF coil, which oscillates at the Larmor frequency of the target nuclei, reorients the net nuclear magnetization of the spins so that a MR signal can be induced and detected by the receive coil. In principle, the effective B_1 fields consist of two components: transmit B_1 (denoted as H_1^+ in this paper), the effective RF magnetic field to induce flip angle of nuclear spin procession, rotating in the same direction of spin procession; receive B_1 (H_1^-), rotating in the opposite direction, also perceived as the receive sensitivity of a receive coil to pick up MR signal. Figure 2 shows vector plots of both B_1 components on an axial plane when, a quadrature volume coil is used (upper row), or a multi-channel transceiver array is used with a single channel for RF power transmission and signal reception (lower row). Note that in RF electromagnetism regime, both magnetic and electric fields generated by the RF coil are complex quantities with magnitude and phase oscillating at the Larmor frequency [54]–[56].

The effect of the B_1 fields on the magnetization of spins and received MR signals can be traced separately to their magnitude and phase. For regular RF pulses at Larmor frequency on resonance, the flip angle of the magnetization from B_0 direction is proportional to the magnitude of the locally transmit B_1 field, while the received MR signal intensity is further weighted by the magnitude of receive B_1 sensitivity, and phase of the complex MR signal is the accumulative phases of both transmit and receive B_1 fields – which is also known as the transceiver phase – and other B_1-independent phase components such as imperfect gradient profile, B_0 variation, chemical shift, etc. Both the excitation of the nuclear magnetization and the reception of signal intensity rely on interactions between applied RF magnetic fields and local electrical properties that can be described by Maxwell's Equations. Therefore, knowing B_1 fields can provide a tangible step towards EPs imaging; feasible and practical B_1-mapping methods have served as the groundwork in EPT studies. On one hand, various B_1-mapping methods have been proposed to measure the magnitude of B_1 components (especially for transmit B_1 component), such as using multiple acquisitions with different flip angles of spins [57], [58], applying identical RF pulses followed by two delays of different repetition times (TRs) [59], utilizing phase-sensitive means based on composite RF pulses [60] or on the Bloch-Siegert phase shift [61], and employing stimulated echoes acquisition mode (STEAM) in multi-pulse sequences [62], [63] or in a single sequence followed by a tailored gradient echo train [64]. On the other hand, there is no direct measurement to quantitatively obtain the absolute phase distribution of the transmit or

receive B_1 field. Instead, the phase information carried in the MR signal phase can be used to infer the absolute phase as will be introduced later in this review.

III. RECONSTRUCTION METHODS

A. Fundamental Electromagnetism Equation

The fundamental theory of EPT is derived from the physical relationship between the distribution of the object's electrical properties and wave propagation of the RF-coil-induced EM fields, as described in Maxwell's Equations. We assume the main magnetic field of the MR scanner is oriented in the *Z*-direction, and consider the magnetic permeability inside biological tissues to be equal to that in vacuum. The RF fields excited in MRI coils at the Larmor frequency of protons can be treated as time-harmonic EM fields [65], [66]. It is also assumed, as in most existing EPT researches, that the electrical properties of the object of interest are isotropic; there have been a few studies investigating EPs anisotropy at Larmor frequency [67], [68], which are beyond the scope of this review. The core equation of EPT, which directly links EPs and RF-coil-induced magnetic fields, can be obtained by combining the Ampere's Law and Faraday's Law as

$$-\nabla^2\mathbf{H}=\omega^2\mu_0\varepsilon_c\mathbf{H}+(\nabla\varepsilon_c/\varepsilon_c)\times(\nabla\times\mathbf{H}) \quad (1)$$

where **H** is the RF-coil-induced magnetic field strength vector in the Cartesian coordinate**,** ω the operating angular frequency (Larmor frequency), $\varepsilon_c = \varepsilon_r\,\varepsilon_0 - i\sigma/\omega$ the complex permittivity as a function of the electrical conductivity σ and the relative permittivity ε_r, ε_0 and μ_0 are the free space permittivity and permeability, respectively.

Eq. (1) provides a theoretical expression of electromagnetic wave equation by directly linking EPs and RF-coil-induced magnetic fields, and thus it serves as the fundamental equation in EPT. Eq. (1) can be simplified according to various assumptions in terms of 1) the spatial variation of EPs and/or 2) spatial RF magnetic field distributions. Although distribution of the Cartesian components of the RF magnetic fields cannot be measured straightforwardly in MRI, the principle of reciprocity [54] links transverse RF magnetic field components in Cartesian and rotating frames. Therefore, the classic EPT problem lies in the course that: simplified Eq. (1) is re-formalized into B_1 terms, i.e. H_1^+ and/or H_1^-, through which EPs can be computed from measurable information of H_1^+ and/or H_1^- distributions, as discussed below.

I. By assuming the EPs distribution is locally homogeneous, Eq. (1) can be simplified and re-organized into the Helmholtz Equation as

$$-\nabla^2 H_1^+=\omega^2\mu_0\varepsilon_c\cdot H_1^+ \quad (2)$$

in which absolute EP values can be directly computed via the fraction derived from measured B_1 fields [40]–[42].

II. The spatial variation of EPs distribution is considered. Other than EP values themselves, which are taken into account only as in Eq. (2), Eq. (1) is further expanded with terms of EPs' gradients as below

$$-\nabla^2 H_1^+ = \omega^2 \mu_0 \varepsilon_c H_1^+ - (\partial H_1^+/\partial z)[(\partial \varepsilon_c/\partial z)/\varepsilon_c] \\ -(\partial H_1^+/\partial x - i\partial H_1^+/\partial y)[(\partial \varepsilon_c/\partial x + i\partial \varepsilon_c/\partial y)/\varepsilon_c] \quad (3)$$

in which the curvature of RF-coil-induced H_z is assumed negligible within coils, e.g. birdcage, transverse electromagnetic (TEM) and microstrip coils, and only the transverse components of RF magnetic fields are taken into account as in [43], [50]. The unknown EPs information, shown as terms associated with ε_c in Eq. (3), can be calculated through solving the linear equations formed by multiple H_1^+ measurements.

B. In Consideration of Measurable RF Magnetic Fields

I) Quadrature Coil Application with Transceiver Phase Assumption—

Measurement of H_1^+ magnitude – $\left|H_1^+\right|$ – has been well-established [59], [61], [62], [64], [69], while there has been so far no generic means for $\left|H_1^-\right|$ measurement. In the meantime, using a quadrature volume coil, *absolute* H_1^+ phase – arg(H_1^+) – can be roughly assumed as half of the transceiver phase [41], [42], that can be obtained from MRI phase image by using refocusing pulse, e.g. spin echo (SE) sequences [44], and by manually removing residual phase components resulted from, e.g., ΔB_0 and gradient-field-induced eddy currents [46]. As such, with retrieved H_1^+ complex information, EPs distribution can be directly reconstructed via Eq. (2). Note that Eq. (2) can be separated into real and imaginary parts, and the conductivity and permittivity can be expressed in the form of $\left|H_1^+\right|$ and arg(H_1^+); it has been found that, to the leading order, the conductivity mainly affects the phase distribution of B_1 fields, while the permittivity mainly affects the magnitude distribution of B_1 fields [41], [44], [49].

II) Multi-channel Transmit Coil Application with B_1 Phase Deduction—

By using a multi-channel transceiver array, employing B_1- mapping methods, e.g. hybrid B_1-mapping technique (merging large and small flip angle data for B_1 mapping) [59], [70]– [73], absolute B_1 phase computation can be attained: abundant B_1 information, i.e. measurable magnitude of H_1^+ and H_1^- for individual coil element, as well as their *relative* phase maps between each coil element, can effectively facilitate their *absolute* phase deduction, so to consolidate subsequent calculations of EPs and/or local SAR. This concept was firstly introduced in [47], [49]. By using simulation data on a realistic human head model, Figure 3 shows the generalized flowchart: using multi-channel transmission, the magnitude and relative phase distributions can be measured for each coil element as illustrated in Fig. 3(a), then their absolute phase can be computed as in Fig. 3(b), and finally the electrical properties can be reconstructed as in Fig. 3(c), while all measurable and retrieved information lead to the ultimate local SAR estimation for each coil element as in Fig. 3(d).

As reported in [47], [51], [74], Eq. (2) was the central equation in *absolute* B_1 phase retrieval and the subsequent EPs reconstruction. In [74], measurable proton-density-biased $\left|H_1^-\right|$ is taken into account, and the phase and EP values can be directly reconstructed altogether – this approach has been named as Local Maxwell Tomography (LMT).

Unlike above approaches which assume locally-homogeneous EPs distribution and may introduce artifacts in the vicinity of tissue boundaries in reconstructed EPs maps, in [49] Gauss's Law has been employed, utilizing the continuously differentiable nature of the magnetic field vector in space, in order to retrieve the *absolute* phase of H_1^+ and H_1^-. The retrieved phases were applied consequently to reconstruct EPs via Eq. (3) [50], removing the piece-wise homogeneous assumption and thus providing a practical way to study complex anatomical structures. Note that to apply Gauss's Law necessitates the knowledge of $\left|H_1^-\right|$; nevertheless, proton density can be estimated on fairly left-right symmetric anatomical structures, e.g. the human brain, about the sagittal plane through the object center [49], [72].

More recently, evolving from Eq. (3), a gradient-based EPT (gEPT) approach was introduced to reconstruct EPs from the estimated gradient of EPs [75]. The central equation of gEPT is

$$\begin{cases} \nabla^2 H_1^+ = -\omega^2 \mu_0 H_1^+ \varepsilon_c + (\nabla H_1^+)^T \begin{bmatrix} 1 & i & 0 \\ -i & 1 & 0 \\ 0 & 0 & 1 \end{bmatrix} (\nabla \ln \varepsilon_c) \\ \nabla^2 H_1^- = -\omega^2 \mu_0 H_1^- \varepsilon_c + (\nabla H_1^-)^T \begin{bmatrix} 1 & -i & 0 \\ i & 1 & 0 \\ 0 & 0 & 1 \end{bmatrix} (\nabla \ln \varepsilon_c) \end{cases} \quad (4)$$

Eq. (4) can be further decomposed into variables including 1) aforementioned known (measurable) variables such as B_1 magnitude and *relative* phase, 2) unknown variables such as ε_c, $\nabla \ln \varepsilon_c$, as well as *absolute* B_1 phase. Utilizing measured multiple B_1 data sets, a set of linear equations can be formed to derive the gradient $\nabla \ln \varepsilon_c$. Then using *a priori* information of the electrical properties, e.g. literature-reported ε_c value(s) at one (or several) specific location(s) with known tissue type(s), quantitative maps of ε_c can be determined through spatial integration across the imaging plane. Taking advantage of derived $\nabla \ln \varepsilon_c$, reduced boundary artifact and improved robustness against noise contamination are anticipated to improve the overall reconstruction performance.

From the perspective of RF coils per se, Eq. (2) based algorithms preserve a generality that they can be implemented on various kinds of coil design, as long as negligible spatial EPs variation pervades locally – dedicated image segmentations such as that in [76] can potentially reduce tissue boundary artifacts in EPT reconstruction. On the other hand, Eqs. (3) and (4) based approaches work well on coils with strip element design (e.g. birdcage, TEM and microstrip coils), in which the spatial variations of RF-coil-induced H_z have been much restrained and thus are reasonably assumed to be negligible compared to those of H_x and H_y.

C. Local SAR Estimation

Local SAR is defined by:

$$\mathrm{SAR}=\sigma(|E_x|^2+|E_y|^2+|E_z|^2)/2\rho \quad (5)$$

where E_x, E_y and E_z are Cartesian components of the RF-coil-induced electric fields, and ρ is material mass density [24], [77], [78]. Note that, by far, the absence of a practical Bz-mapping method – measuring the *z*-component of RF-coil-induced magnetic fields that does not contribute to nuclear precession – limits the computation of the full components of RF-coil-induced electric fields, and only E_z component can be calculated theoretically from measured/estimated transverse components of RF magnetic fields (B_1) via Ampere's Law. As a consequence, it constrains current SAR estimation methods due to incomplete information of the full components of RF electric fields. Nevertheless, for RF coils (e.g. birdcage, TEM and microstrip coils), E_z dominates the electric field due to the coil structure [42], [43], [47], [49], [50], [79], thus only E_z component is considered in local SAR estimation. Since local E_z can be derived as a function of H_1^+ and H_1^- according to Ampere's Law, measuring/estimating the complex B_1 distribution and reconstructing EPs values through the course of EPT calculation allow for efficient estimation of subject-specific and real-time local SAR [50].

IV. EXPERIMENT STUDIES: A HISTORIC REVIEW

A. Phantom Validations

The first phantom validation has been conducted on 1.5T and 4.7T MRI machines as reported in [41]. With the mapping of $\left|H_1^+\right|$ and transceiver phase, by utilizing the transceiver phase assumption, good agreement was reached between known and measured EP values of saline phantoms with different concentrations. The piecewise-homogeneous Helmholtz equation as in Eq. (2) was used as the reconstruction equation. In addition, it has also been shown that the increased wave propagation effects at 4.7T allowed improved spatial resolution and better measurement accuracy compared to 1.5T.

Originating from the Helmholtz equation, the phase-based conductivity imaging and magnitude-based permittivity imaging methods have been proposed, and its feasibility has been tested using a saline phantom on a 1.5T MRI machine equipped with a quadrature head coil [44]. Reasonable experimental results revealed that the phase-based approximation works well in the case of $\omega\varepsilon \ll \sigma$, while magnitude-based approximation suits better when $\omega\varepsilon \gg \sigma$. The simplified method, especially phase-based conductivity imaging, holds promise towards clinical applications due to its potential merits in shortened scan time as well as preserved reconstruction stability.

Built upon above work, fast phase-based conductivity imaging has been tested in a saline phantom to monitor the dynamic change in conductivity along the time course when salt was added during a 1.5T scan. An SSFP (steady-state free-precession) sequence was utilized, and the scan time was reduced from the order of minutes to several seconds. The real-time reconstruction results preserve good quality [80]. An extensive study has been conducted to

further investigate the effect of B_0 strength for Helmholtz-based EPT at 1.5, 3 and 7T on a head-shaped phantom [52], and it was concluded that using Eq. (2) based approach: 1) the transceiver phase assumption is more reliable for lower-field MRI (i.e. 1.5T and 3T) and on object with lower permittivity and with symmetric structure (about the sagittal plane through the center), 2) the phase-based conductivity imaging mainly preserves its feasibility at 1.5T and 3T, and 3) the precision of EPT reconstruction (especially for permittivity) benefits from a higher B_0 strength, which is associated with increased B_1 SNR and more prominent curvature of B_1 distribution (in the consideration of spatial differential computation involved in EPT algorithms).

Using multi-channel transmit technique, Eq. (2) based methods have been tested on single-compartment saline phantoms, and reasonable EPs results [47], [74], [49]–[51] suggest that reliable B_1 phase calculation and EPs reconstruction can be achieved through mathematical deductions, instead of being limited to quadrature coil application which suffers from diminished accuracy of coil-dependent transceiver phase approximation, as well as intrinsic and prominent B_1 inhomogeneity at UHF MRI. Successful implementations with non-quadrature coils would substantially expand the applicability of EPT for future clinical applications.

B. In vivo Brain EPs Imaging

Most *in vivo* EPT studies have focused on brain imaging of healthy subjects. The first *in vivo* study was performed in six subjects at 1.5T [44]: average EP values inside regions of interest (ROI), i.e. grey matter (GM), white matter (WM) and cerebrospinal fluid (CSF), showed good agreement with literature values, while up to 15%~20% differences in reconstructed EP results were observed among subjects. The quadrature-dependent transceiver phase assumption was utilized in Helmholtz-based algorithm, and it has been further evaluated in [52] on a single human subject at 1.5T, 3T and 7T: 1) the transceiver phase error was found minimal at 3T and maximal at 7T in the head; 2) elevated reconstructed conductivity was produced at 7T compared with 1.5T and 3T when using phase-based method, while 1.5T and 3T showed inferior permittivity reconstruction results due to higher noise levels observed at lower B_0 field; 3) boundary artifacts were observed in all reconstructed EP maps due to piece-wise homogeneous assumption when employing the Helmholtz-based algorithm.

At 7T, the first *in vivo* human study using multi-channel transceiver technique has been reported in [49], in which aforementioned approximate symmetry nature of human brain and Gauss's Law-based B_1 phase retrieval method were utilized to estimate the full complex information of B_1. As an example, Figure 4 depicts, on the transverse slice of interest, computed phase gradients of transmit and receive B_1 for a selected reference coil element, as well as their phase difference. Reconstructed EP maps for one subject are shown in [49], and the CSF in the lateral ventricle can be observed in shape, while the average bias and standard deviation for reconstructed conductivity *in vivo* were 28% and 67%, and 10% and 43% for relative permittivity, respectively. Most recently, employing the same B_1-mapping technique at 7T [70], [71], [81], [82], the gEPT approach based on Eq. (4) has been tested in a human subject, in which $\nabla \ln \varepsilon_c$ was derived and further integrated in space to produce *in*

vivo EP maps [75]. Figure 5 [75] presents the reconstructed maps of conductivity as in Fig. 5(b) and permittivity in Fig. 5(c), both exhibiting clear anatomical boundaries and brain structures in comparison with the T1-weighted image shown in Fig. 5(a). Reconstructed EP values are close to literature reported values at 300MHz.

By using Eq. (2) based method with quadrature B_1 measurement and transceiver phase assumption, several cases of brain tumors (i.e. brain glioma, grade II and IV astrocytoma) have been studied at 1.5T and 7T, and it was reported with a >150% higher electrical conductivity compared to the surrounding white matter [83], [84]. Twelve patients with primary brain tumor, metastases and resected primary brain tumor have been examined at 1.5T and 3T using SSFP, and several findings have been reported: supratentorial localized primary brain tumors consistently showed higher conductivity than healthy supratentorial white matter, while infratentorial tumors showed lower or equivalent conductivity values compared to healthy infratentorial white matter; phylogenetic older parts, e.g. basal ganglia and the cerebellum, showed higher conductivity compared to the cerebrum as a phylogenetic newer part [85]. A single patient with ischemic stroke has also been studied at 7T, and the reconstructed conductivity showed local increase in the region containing tissues affected by the infarction [86].

C. In vivo Body EPs Imaging

Liver conductivity imaging has been performed over ten healthy subjects during a single breath hold at 1.5T [87] by applying the similar method reported in [80]. Reconstructed results showed good agreement with literature values. Artifacts were presumably attributed to transferred cardiac motion, blood flow and perfusion effects, and may also result from the piece-wise homogeneous assumption applied in Eq. (2).

A single patient with breast cancer was studied at 3T [76]. Considering significant variations in conductivity values among breast tissues, e.g. gland and fat, image segmentation was implemented for shaping the kernel when applying Eq. (2), and parabola-fitting was used to restrain boundary artifacts. As shown in Figure 6 [76], much higher conductivity was found in cancerous tumor, while moderately higher values were found in cysts compared to the surrounding fat. A following study has been conducted over eight patients with breast-containing lesion, including four classified as malignant and four as benign, and significant maxima in suspicious areas were observed: the conductivity of all benign lesions are below ~2–3 S/m, one malignant lesion below ~2 S/m, and the other three malignant tumors exhibited elevated values of up to ~4–6 S/m [88], compared to typical thymus conductivity value of ~0.8 S/m at the operating frequency [1]–[3]. High EP values of breast cancer tissue has also been reported in [89], [90].

D. In vivo SAR Estimation

Using the Helmholtz-based algorithm and transceiver phase assumption, *in vivo* local SAR mapping using quadrature coil at 1.5T and 3T has been reported in human brain imaging [79]. Estimated local SAR revealed overall similar structure with simulated distribution. Maximum 10-gram average local SAR values showed lower value than those obtained from simulation, e.g. 25–55% lower at 1.5T.

However, elevated energy deposition is intrinsically associated with increased operating frequency, resulting in higher local heating and thus causing a more serious safety concern at UHF. While multiple-channel transmission has been widely recognized in its advantage in B_1 inhomogeneity compensation at UHF, real-time and subject-specific local SAR quantification and management under international safety guidelines are highly desirable to fully unfold its potentials in B_1 shimming or parallel transmission to attain superior MRI images at UHF. Towards this goal, built upon their recent work on complex B_1 imaging [49] and Eq. (3)- based EPT algorithm [43], *in vivo* single-coil-element local SAR mapping has been recently reported using a multi-channel transceiver array coil at 7T in human brain imaging [50]. Estimated voxel-wise local SAR distributions on two subjects exhibited patterns with reasonable similarity compared with simulation results, as shown in Figure 7 [91], and noticeable differences may result from certain factors in numerical modeling, such as coil coupling, head anatomical structure and assumption of dominant E_z. This approach holds promises for enabling subject-specific local SAR computation which in turn can be used as explicit constraint in B_1 shimming calculation and parallel transmission RF pulse design.

V. FUTURE PROSPECT AND CONCLUSION

Electrical properties are passive tissue properties. When external electric fields are exerted, electric currents flow and magnetic fields are induced inside the object. Electrical Properties Tomography (EPT) exploits the highly nonlinear relationship between tissues' electrical properties and resulted RF magnetic fields, reconstructing conductivity and permittivity images through investigating the underlying physical principles, i.e. Maxwell's Equations and MR physics. Only B_1 maps – the curvature distributions inside the object that can be noninvasively measured *in vivo* by an MRI scanner – are required for subsequent computations, thus well-posed reconstruction problems can be formulated and hereby high-resolution EP images can be produced. Compared with other EPs imaging technique, EPT has certain advantages including its non-invasiveness, high spatial resolution and superior feasibility for *in vivo* study. In the past several years, there has been a blossom of EPT studies covering a broad spectrum of investigations over the MRI measurement techniques and correlated inverse algorithms.

Along the development of EPT, more accurate EPs reconstruction has been pursued. Although piece-wise homogeneous assumption can be locally applied after careful manual tissue segmentation, its complexity and performance, when extending EPT to whole body application and over tissues with complicated anatomical structures, deserve further investigation and evaluation [45]. Several studies have devoted efforts focusing on inhomogeneous EPs distribution. For example, methods reported in [49], [50], [75] originate from the Gauss's Law for magnetism by utilizing the continuously differentiable nature of the magnetic field vector in space, and the spatial variation of EPs distribution is taken into account in the central inverse equation; the recently proposed gEPT approach [75] demonstrates superior performance in *in vivo* brain EPs imaging, suggesting the high quality of EPs imaging one can anticipate. In the meantime, through simulation evaluations and phantom validations, there have also been several pilot studies to deal with such boundary issues towards refined EP image reconstruction [92]–[95]; whether they can be successfully

applied to *in vivo* studies is yet under investigation. Future works are needed to develop generic EPT algorithms, which should be independent of anatomy structure, RF coil design, and B_0 field strength.

Local SAR calculation requires frequency-dependent electrical properties of local tissues, as well as locally distorted electric fields – both of which are subject-specific. Differing from other EPs imaging modalities, EPT studies EP values at the operating Larmor frequency, with which the local electric fields can be directly deducted from measured B_1. In addition, unlike external model-based SAR simulation methods that are based on a few human models (i.e., not derived on a per subject basis) and are highly time-consuming, the EPT approach begins with B_1-mapping *in vivo*, and further calculate EPs and electric fields, overarching all associated quantities on a subject-specific basis, and may also allow for fast real-time SAR calculation. Furthermore, EPT-based SAR estimation can account for positions of subjects relative to the RF coil during an MRI scan, which, on the contrary, is unpredictable in SAR calculation based on computational EM simulation. As documented in [50] and in agreement with [96], significant SAR estimation discrepancies can be introduced with a trivial position offset. This suggests that the EPT based approach, which does not require or rely heavily on accurate 3-D modeling (in terms of model structure and position), preserves certain merits being subject-specific. As reported in [50], *in vivo* SAR estimation results for brain imaging are encouraging, suggesting real-time local SAR prediction for a specific human subject may be eventually feasible, relying only on measurable B_1 information (i.e., magnitude and relative phase). It is anticipated that future studies will provide generalized estimation of absolute B_1 phase and EPs map, independent of the current assumption of negligible Bz component; and ultimately, full components of RF-coil-induced EM fields can be fully measured/retrieved, furnishing EPT with complete electric fields information towards more accurate and reliable SAR estimation.

Lastly but importantly, B_1-mapping techniques play an important role on the overall performance of EPT in terms of, e.g. image resolution, the reliability and accuracy of reconstruction results. As illustrated above in the method section, a series of mathematical deduction involved in EPT reconstruction steps requires B_1 maps with desirable qualities such as high SNR in the region of interest, minimally biased by various tissue properties (e.g. T1, T2*, proton density, blood flow, etc.), largely robust against chemical shift (i.e. in fat tissue) and body motion. In general, precise B_1-mapping within a practically fast acquisition time deserves relentless pursuing for future promising clinical applications of EPT.

In summary, MR based Electrical Properties Tomography represents an important development in our efforts to map the electrical properties of biological tissues, which promises to have important clinical applications including cancer detection and diagnosis, as well as bettering management of MR safety through subject-specific real time SAR estimation. The establishment of Electrical Properties Tomography may also play a significant role in managing subject safety in high field or ultra-high field MRI, thus maximizing its clinical potential.

Acknowledgments

This work was supported in part by NIH RO1EB006433, RO1EB007920, R21EB017069, R21EB009133, R21EB014353, P41RR008079, P30NS057091, and U01HL117664.

The authors are grateful to Drs. P.-F. Van de Moortele and S. Schmitter for useful discussions.

References

1. Gabriel C, Gabriel S, Corthout E. The dielectric properties of biological tissues: I. Literature survey. Phys Med Biol. Nov.1996 41:2231–2249. [PubMed: 8938024]
2. Gabriel S, Lau RW, Gabriel C. The dielectric properties of biological tissues: II. Measurements in the frequency range 10 Hz to 20 GHz. Phys Med Biol. Nov; 1996 41(11):2251–2269. [PubMed: 8938025]
3. Gabriel S, Lau RW, Gabriel C. The dielectric properties of biological tissues: III. Parametric models for the dielectric spectrum of tissues. Phys Med Biol. Nov; 1996 41(11):2271–2293. [PubMed: 8938026]
4. Fricke H. The Electric Capacity of Suspensions with Special Reference to Blood. J Gen Physiol. Nov; 1925 9(2):137–152. [PubMed: 19872238]
5. Foster KR, Schwan HP. Dielectric properties of tissues and biological materials: a critical review. Crit Rev Biomed Eng. 1989; 17(1):25–104. [PubMed: 2651001]
6. Joines WT. The measured electrical properties of normal and malignant human tissues from 50 to 900 MHz. Med Phys. 1994; 21(4):547–550. [PubMed: 8058021]
7. Stojadinovic A, Nissan A, Gallimidi Z, Lenington S, Logan W, Zuley M, Yeshaya A, Shimonov M, Melloul M, Fields S, Allweis T, Ginor R, Gur D, Shriver CD. Electrical impedance scanning for the early detection of breast cancer in young women: preliminary results of a multicenter prospective clinical trial. J Clin Oncol Off J Am Soc Clin Oncol. Apr; 2005 23(12):2703–2715.
8. Surowiec AJ, Stuchly SS, Barr JR, Swarup A. Dielectric properties of breast carcinoma and the surrounding tissues. IEEE Trans Biomed Eng. 1988; 35(4):257–263. [PubMed: 2834285]
9. Morimoto T, Kinouchi Y, Iritani T, Kimura S, Konishi Y, Mitsuyama N, Komaki K, Monden Y. Measurement of the Electrical Bio-Impedance of Breast Tumors. Eur Surg Res. 1990; 22(2):86–92. [PubMed: 2384126]
10. Jossinet J, Schmitt M. A Review of Parameters for the Bioelectrical Characterization of Breast Tissue. Ann N Y Acad Sci. 1999; 873(1):30–41. [PubMed: 10372147]
11. Wilkinson BA, Smallwood RH, Keshtar A, Lee JA, Hamdy FC. Electrical Impedance Spectroscopy and the Diagnosis of Bladder Pathology: A Pilot Study. J Urol. Oct; 2002 168(4 Part 1):1563–1567. [PubMed: 12352458]
12. Fear EC, Li X, Hagness SC, Stuchly MA. Confocal microwave imaging for breast cancer detection: localization of tumors in three dimensions. IEEE Trans Biomed Eng. 2002; 49(8):812–822. [PubMed: 12148820]
13. Zou Y, Guo Z. A review of electrical impedance techniques for breast cancer detection. Med Eng Phys. Mar; 2003 25(2):79–90. [PubMed: 12538062]
14. Poplack SP, Paulsen KD, Hartov A, Meaney PM, Pogue BW, Tosteson TD, Grove MR, Soho SK, Wells WA. Electromagnetic Breast Imaging: Average Tissue Property Values in Women with Negative Clinical Findings. Radiology. May; 2004 231(2):571–580. [PubMed: 15128998]
15. Poplack SP, Tosteson TD, Wells WA, Pogue BW, Meaney PM, Hartov A, Kogel CA, Soho SK, Gibson JJ, Paulsen KD. Electromagnetic Breast Imaging: Results of a Pilot Study in Women with Abnormal Mammograms. Radiology. May; 2007 243(2):350–359. [PubMed: 17400760]
16. Lazebnik M, Zhu C, Palmer GM, Harter J, Sewall S, Ramanujam N, Hagness SC. Electromagnetic Spectroscopy of Normal Breast Tissue Specimens Obtained From Reduction Surgeries: Comparison of Optical and Microwave Properties. IEEE Trans Biomed Eng. 2008; 55(10):2444–2451. [PubMed: 18838370]
17. Hassan AM, El-Shenawee M. Review of Electromagnetic Techniques for Breast Cancer Detection. Biomed Eng IEEE Rev. 2011; 4:103–118.

18. Aberg P, Nicander I, Hansson J, Geladi P, Holmgren U, Ollmar S. Skin cancer identification using multifrequency electrical impedance-a potential screening tool. IEEE Trans Biomed Eng. 2004; 51(12):2097– 2102. [PubMed: 15605856]
19. Halter RJ, Hartov A, Heaney JA, Paulsen KD, Schned AR. Electrical Impedance Spectroscopy of the Human Prostate. IEEE Trans Biomed Eng. 2007; 54(7):1321–1327. [PubMed: 17605363]
20. Halter RJ, Schned A, Heaney J, Hartov A, Schutz S, Paulsen KD. Electrical Impedance Spectroscopy of Benign and Malignant Prostatic Tissues. J Urol. Apr; 2008 179(4):1580–1586. [PubMed: 18295258]
21. Halter RJ, Schned A, Heaney J, Hartov A, Paulsen KD. Electrical Properties of Prostatic Tissues: I. Single Frequency Admittivity Properties. J Urol. Oct; 2009 182(4):1600–1607. [PubMed: 19683745]
22. Uğurbil K, Adriany G, Andersen P, Chen W, Garwood M, Gruetter R, Henry P-G, Kim S-G, Lieu H, Tkac I, Vaughan T, Van De Moortele P-F, Yacoub E, Zhu X-H. Ultrahigh field magnetic resonance imaging and spectroscopy. Magn Reson Imaging. Dec; 2003 21(10):1263–1281. [PubMed: 14725934]
23. Lattanzi R, Sodickson DK, Grant AK, Zhu Y. Electrodynamic constraints on homogeneity and radiofrequency power deposition in multiple coil excitations. Magn Reson Med. 2009; 61(2):315–334. [PubMed: 19165885]
24. Collins CM, Liu W, Wang J, Gruetter R, Vaughan JT, Ugurbil K, Smith MB. Temperature and SAR calculations for a human head within volume and surface coils at 64 and 300 MHz. J Magn Reson Imaging JMRI. May; 2004 19(5):650–656.
25. Kopanoglu E, Erturk VB, Atalar E. Analytic expressions for the ultimate intrinsic signal-to-noise ratio and ultimate intrinsic specific absorption rate in MRI. Magn Reson Med. 2011; 66(3):846–858. [PubMed: 21394773]
26. Metherall P, Barber DC, Smallwood RH, Brown BH. Three-dimensional electrical impedance tomography. Nature. 1996; 380(6574):509–512. [PubMed: 8606768]
27. Mueller JL, Isaacson D, Newell JC. A reconstruction algorithm for electrical impedance tomography data collected on rectangular electrode arrays. Biomed Eng IEEE Trans. Nov; 1999 46(11):1379–1386.
28. Korzhenevskii AV, Cherepenin VA. Magnetic induction tomography. J Commun Technol Electron. 42(4):469–474.
29. Griffiths H, Stewart WR, Gough W. Magnetic Induction Tomography: A Measuring System for Biological Tissues. Ann N Y Acad Sci. Apr; 1999 873(1):335–345. [PubMed: 10372181]
30. Joy M, Scott G, Henkelman M. In vivo detection of applied electric currents by magnetic resonance imaging. Magn Reson Imaging. 1989; 7(1):89–94. [PubMed: 2918822]
31. Scott GC, Joy MLG, Armstrong RL, Henkelman RM. RF Current Density Imaging in Homogeneous Media. Magn Reson Med. Dec; 1992 28(2):186–201. [PubMed: 1461122]
32. Zhang, N. MS thesis. Univ. Toronto; Toronto, ON, Canada: 1992. Electrical Impedance Tomography Based on Current Density Imaging.
33. Kwon O, Woo EJ, Yoon JR, Seo JK. Magnetic resonance electrical impedance tomography (MREIT): simulation study of J-substitution algorithm. IEEE Trans Biomed Eng. Feb; 2002 49(2): 160–167. [PubMed: 12066883]
34. Gao N, Zhu SA, He B. Estimation of electrical conductivity distribution within the human head from magnetic flux density measurement. Phys Med Biol. Jun; 2005 50(11):2675–2687. [PubMed: 15901962]
35. Gao N, He B. Noninvasive Imaging of Bioimpedance Distribution by Means of Current Reconstruction Magnetic Resonance Electrical Impedance Tomography. IEEE Trans Biomed Eng. 2008; 55(5):1530–1538. [PubMed: 18440899]
36. Wen H, Shah J, Balaban RS. Hall effect imaging. IEEE Trans Biomed Eng. 1998; 45(1):119– 124. [PubMed: 9444846]
37. Xu Y, He B. Magnetoacoustic tomography with magnetic induction (MAT-MI). Phys Med Biol. Nov; 2005 50(21):5175–5187. [PubMed: 16237248]

38. Li X, Xu Y, He B. Imaging Electrical Impedance From Acoustic Measurements by Means of Magnetoacoustic Tomography With Magnetic Induction (MAT-MI). IEEE Trans Biomed Eng. Feb; 2007 54(2):323–330. [PubMed: 17278589]
39. Mariappan L, Li X, He B. B-scan based acoustic source reconstruction for magnetoacoustic tomography with magnetic induction (MAT-MI). IEEE Trans Biomed Eng. Mar; 2011 58(3):713–720. [PubMed: 21097372]
40. Haacke EM, Petropoulos LS, Nilges EW, Wu DH. Extraction of conductivity and permittivity using magnetic resonance imaging. Phys Med Biol. Jun; 1991 36(6):723–734.
41. Wen, H. Noninvasive quantitative mapping of conductivity and dielectric distributions using RF wave propagation effects in high-field MRI. Proc. of SPIE; San Diego, CA, USA. 2003. p. 471-477.
42. Katscher U, Voigt T, Findeklee C, Vernickel P, Nehrke K, Dossel O. Determination of Electric Conductivity and Local SAR Via B1 Mapping. Med Imaging IEEE Trans. Sep; 2009 28(9):1365–1374.
43. Zhang X, Zhu S, He B. Imaging Electric Properties of Biological Tissues by RF Field Mapping in MRI. IEEE Trans Med Imaging. Feb; 2010 29(2):474– 481. [PubMed: 20129847]
44. Voigt T, Katscher U, Doessel O. Quantitative conductivity and permittivity imaging of the human brain using electric properties tomography. Magn Reson Med. 2011; 66(2):456–466. [PubMed: 21773985]
45. Seo JK, Kim MO, Lee J, Choi N, Woo EJ, Kim HJ, Kwon OI, Kim DH. Error analysis of nonconstant admittivity for MR-based electric property imaging. IEEE Trans Med Imaging. Feb; 2012 31(2):430– 437. [PubMed: 21990329]
46. van Lier AL, Brunner DO, Pruessmann KP, Klomp DWJ, Luijten PR, Lagendijk JJW, van den Berg CAT. B1+ Phase mapping at 7 T and its application for in vivo electrical conductivity mapping. Magn Reson Med. 2012; 67(2):552–561. [PubMed: 21710613]
47. Katscher U, Findeklee C, Voigt T. B1-based specific energy absorption rate determination for nonquadrature radiofrequency excitation. Magn Reson Med. 2012; 68(6):1911–1918. [PubMed: 22374804]
48. Bulumulla SB, Lee SK, Yeo TBD. Conductivity and permittivity imaging at 3.0 t. Concepts Magn Reson Part B Magn Reson Eng. 2012; 41B(1):13–21. [PubMed: 23599691]
49. Zhang X, de Moortele PFV, Schmitter S, He B. Complex B1 mapping and electrical properties imaging of the human brain using a 16-channel transceiver coil at 7T. Magn Reson Med. 2013; 69(5):1285–1296. [PubMed: 22692921]
50. Zhang X, Schmitter S, Van de Moortele P, Liu J, He B. From Complex B1 Mapping to Local SAR Estimation for Human Brain MR Imaging Using Multi- Channel Transceiver Coil at 7T. IEEE Trans Med Imaging. 2013; 32(6):1058–1067. [PubMed: 23508259]
51. Liu J, Zhang X, Van de Moortele PF, Schmitter S, He B. Determining electrical properties based on B(1) fields measured in an MR scanner using a multi-channel transmit/receive coil: a general approach. Phys Med Biol. Jul; 2013 58(13):4395–4408. [PubMed: 23743673]
52. van Lier ALHMW, Raaijmakers A, Voigt T, Lagendijk JJW, Luijten PR, Katscher U, van den Berg CAT. Electrical Properties Tomography in the Human Brain at 1.5, 3, and 7T: A Comparison Study. Magn Reson Med. 2013 n/a–n/a.
53. Buchenau S, Haas M, Splitthoff DN, Hennig J, Zaitsev M. Iterative separation of transmit and receive phase contributions and B1+-based estimation of the specific absorption rate for transmit arrays. Magn Reson Mater Phys Biol Med. 2013:1–14.
54. Hoult DI. The principle of reciprocity in signal strength calculations—A mathematical guide. Concepts Magn Reson. Jan; 2000 12(4):173–187.
55. Milles J, Zhu YM, Chen NK, Panych LP, Gimenez G, Guttmann RG. Computation of Transmitted and Received Fields in Magnetic Resonance Imaging. IEEE Trans Biomed Eng. 2006; 53(5):885–895. [PubMed: 16686411]
56. Collins CM, Wang Z. Calculation of radiofrequency electromagnetic fields and their effects in MRI of human subjects. Magn Reson Med. 2011; 65(5):1470–1482. [PubMed: 21381106]
57. Insko EK, Bolinger L. Mapping of the radiofrequency field. J Magn Reson A. 1993; 103(1):82–85.

58. Wang J, Qiu M, Yang QX, Smith MB, Constable RT. Measurement and correction of transmitter and receiver induced nonuniformities in vivo. Magn Reson Med. 2005; 53(2):408–417. [PubMed: 15678526]
59. Yarnykh VL. Actual flip-angle imaging in the pulsed steady state: A method for rapid three-dimensional mapping of the transmitted radiofrequency field. Magn Reson Med. Jan; 2007 57(1): 192–200. [PubMed: 17191242]
60. Morrell GR. A phase-sensitive method of flip angle mapping. Magn Reson Med. 2008; 60(4):889–894. [PubMed: 18816809]
61. Sacolick LI, Wiesinger F, Hancu I, Vogel MW. B1 mapping by Bloch-Siegert shift. Magn Reson Med. 2010; 63(5):1315–1322. [PubMed: 20432302]
62. Akoka S, Franconi F, Seguin F, Le Pape A. Radiofrequency map of an NMR coil by imaging. Magn Reson Imaging. 1993; 11(3):437–441. [PubMed: 8505878]
63. Helms G, Finsterbusch J, Weiskopf N, Dechent P. Rapid radiofrequency field mapping in vivo using single-shot STEAM MRI. Magn Reson Med. 2008; 60(3):739–743. [PubMed: 18727090]
64. Nehrke K, Börnert P. DREAM—a novel approach for robust, ultrafast, multislice B1 mapping. Magn Reson Med. 2012; 68(5):1517–1526. [PubMed: 22252850]
65. Ibrahim TS, Mitchell C, Abraham R, Schmalbrock P. In-depth study of the electromagnetics of ultrahigh-field MRI. NMR Biomed. 2007; 20(1):58–68. [PubMed: 17006885]
66. Collins CM. Numerical field calculations considering the human subject for engineering and safety assurance in MRI. NMR Biomed. 2009; 22(9):919–926. [PubMed: 18384179]
67. Katscher, U.; Voigt, T.; Findeklee, C. Estimation of the Anisotropy of Electric Conductivity via B1 Mapping. Proc. of ISMRM; Stockholm, Sweden. 2010. p. 2866
68. Lee J, Song Y, Choi N, Cho S, Seo JK, Kim D-H. Noninvasive Measurement of Conductivity Anisotropy at Larmor Frequency Using MRI. Comput Math Methods Med. Mar.2013 2013
69. Insko EK, Bolinger L. Mapping of the radiofrequency field. J Magn Reson A. 103(1):82–85.
70. Van de Moortele PF, Akgun C, Adriany G, Moeller S, Ritter J, Collins CM, Smith MB, Vaughan JT, Uğurbil K. B1 destructive interferences and spatial phase patterns at 7 T with a head transceiver array coil. Magn Reson Med. Dec; 2005 54(6):1503–1518. [PubMed: 16270333]
71. Van de Moortele, P-F.; Snyder, C.; DelaBarre, L.; Adriany, G.; Vaughan, T.; Ugurbil, K. Calibration Tools for RF Shim at Very High Field with Multiple Element RF Coils: from Ultra Fast Local Relative Phase to Absolute Magnitude B1+ Mapping. Proc. of ISMRM; Berlin, Germany. 2007. p. 1676
72. Van de Moortele, P-F.; Uğurbil, K. Very Fast Multi Channel B1 Calibration at High Field in the Small Flip Angle Regime. Proc. of ISMRM; Hawaii, USA. 2009. p. 367
73. Brunner DO, Pruessmann KP. B 1+ interferometry for the calibration of RF transmitter arrays. Magn Reson Med. 2009; 61(6):1480–1488. [PubMed: 19353666]
74. Sodickson, D.; Alon, L.; Deniz, C.; Brown, B.; Zhang, B.; Wiggins, G.; Cho, G.; Eliezer, N.; Novikov, D.; Lattanzi, R.; Duan, Q.; Sodickson, L.; Zhu, Y. Local Maxwell Tomography Using Transmit-Receive Coil Arrays for Contact-Free Mapping of Tissue Electrical Properties and Determination of Absolute RF Phase. Proc. of ISMRM; Melbourne, Australia. 2012. p. 387
75. Liu, J.; Zhang, X.; Schmitter, S.; Van De Moortele, P-F.; He, B. In vivo Imaging of Electrical Properties of Human Brain Using a Gradient Based Algorithm. Proc. of ISMRM; Salt Lake City, USA. 2013. p. 463
76. Katscher, U.; Djamshidi, K.; Voigt, T.; Ivancevic, M.; Abe, H.; Newstead, G.; Keupp, J.; Research, Philips. Estimation of Breast Tumor Conductivity using Parabolic Phase Fitting. Proc. of ISMRM; Melbourne, Australia. 2012. p. 3482
77. Simunic D, Wach P, Renhart W, Stollberger R. Spatial distribution of high-frequency electromagnetic energy in human head during MRI: numerical results and measurements. IEEE Trans Biomed Eng. 1996; 43(1):88. [PubMed: 8567009]
78. Chen J, Feng Z, Jin JM. Numerical simulation of SAR and B1-field inhomogeneity of shielded RF coils loaded with the human head. IEEE Trans Biomed Eng. 1998; 45(5):650–659. [PubMed: 9581064]

79. Voigt T, Homann H, Katscher U, Doessel O. Patient-individual local SAR determination: In vivo measurements and numerical validation. Magn Reson Med. 2012; 68(4):1117–1126. [PubMed: 22213053]
80. Stehning, C.; Voigt, T.; Katscher, U. Real-Time Conductivity Mapping using Balanced SSFP and Phase-Based Reconstruction. Proc. of ISMRM; Montreal, Canada. 2011. p. 128
81. Adriany G, Van de Moortele PF, Ritter J, Moeller S, Auerbach EJ, Akgün C, Snyder CJ, Vaughan T, Uğurbil K. A geometrically adjustable 16-channel transmit/receive transmission line array for improved RF efficiency and parallel imaging performance at 7 Tesla. Magn Reson Med. Mar; 2008 59(3):590–597. [PubMed: 18219635]
82. Van de Moortele PF, Auerbach EJ, Olman C, Yacoub E, Uğurbil K, Moeller S. T1 weighted brain images at 7 Tesla unbiased for Proton Density, T2* contrast and RF coil receive B1 sensitivity with simultaneous vessel visualization. Neuroimage. Jun; 2009 46(2):432–446. [PubMed: 19233292]
83. Voigt, T.; Vaterlein, O.; Stehning, C.; Katscher, U.; Fiehler, J. In vivo Glioma Characterization using MR Conductivity Imaging. Proc. of ISMRM; Montreal, Canada. 2011. p. 127
84. van Lier, AL.; Hoogduin, JM.; Polders, DL.; Boer, VO.; Hendrikse, J.; Robe, PA.; Woerdeman, PA.; Lagendijk, JJ.; Luijten, PR.; van den Berg, CA. Electrical conductivity imaging of brain tumours. Proc. of ISMRM; Montreal, Canada. 2011. p. 4464
85. Huhndorf, M.; Stehning, C.; Rohr, A.; Helle, M.; Katscher, U.; Jansen, O. Systematic Brain Tumor Conductivity Study with Optimized EPT Sequence and Reconstruction Algorithm. ISMRM; Salt Lake City, USA: 2013. p. 3626
86. van Lier, ALHMW.; van der Kolk, AG.; Brundel, M.; Hendrikse, J.; Luijten, PR.; Lagendijk, JJW.; van den Berg, CAT. Electrical conductivity in ischemic stroke at 7.0 Tesla: A Case Study. Proc. of ISMRM; Melbourne, Australia. 2012. p. 3484
87. Stehning, C.; Voigt, T.; Karkowski, P.; Katscher, U.; Research, Philips. Electric Properties Tomography (EPT) of the Liver in a Single Breathhold Using SSFP. Proc. of ISMRM; 2012. p. 386
88. Katscher, U.; Abe, H.; Ivancevic, M.; Djamshidi, K.; Karkowski, P.; Newstead, G. Systematic Brain Tumor Conductivity Study with Optimized EPT Sequence and Reconstruction Algorithm. Proc. of ISMRM; Salt Lake City, USA. 2013. p. 3372
89. Bulumulla, SB.; Hancu, I. Breast permittivity imaging. Proc. of ISMRM; Melbourne, Australia. 2012. p. 2532
90. Shin, J.; Kim, MJ.; Lee, J.; Kim, M.; Choi, N.; Nam, Y.; Kim, DH. Systematic Brain Tumor Conductivity Study with Optimized EPT Sequence and Reconstruction Algorithm. Proc. of ISMRM; Salt Lake City, USA. 2013. p. 4180
91. Zhang, X.; Schmitter, S.; Liu, J.; Van De Moortele, P-F.; He, B. Local SAR Estimation for Human Brain Imaging Using Multi-channel Transceiver Coil at 7T. Proc. of ISMRM; Salt Lake City, USA. 2013. p. 288
92. Hafalir, FS.; Oran, OF.; Gurler, N.; Ider, YZ. Magnetic Resonance Electrical Properties Tomography (MREPT) Based on the Solution of the Convection-Reaction Equation. ISMRM; Salt Lake City, USA: 2013. p. 4187
93. Lee, J.; Choi, N.; Seo, JK.; Kim, D-H. Reduction of boundary artifact in electrical property mapping using MREPT. Proc. of ISMRM; Salt Lake City, USA. 2013. p. 4183
94. Balidemaj, E.; Remis, RF.; van Lier, AL.; Crezee, J.; Sbrizzi, A.; Stalpers, LJA.; van den Berg, CAT. CSI-EPT: A novel Contrast Source Inversion approach to EPT and patient-specific SAR based on B1+ maps. Proc. of ISMRM; Salt Lake City, USA. 2013. p. 4185
95. Sodickson, D.; Alon, L.; Deniz, C.; Ben-Eliezer, N.; Cloos, M.; Sodickson, L.; Collins, CM.; Wiggins, G.; Novikov, D. Generalized Local Maxwell Tomography for Mapping of Electrical Property Gradients and Tensors. Proc. of ISMRM; Salt Lake City, USA. 2013. p. 4175
96. Wolf S, Diehl D, Gebhardt M, Mallow J, Speck O. SAR simulations for high-field MRI: How much detail, effort, and accuracy is needed? Magn Reson Med. 2013; 69(4):1157–1168. [PubMed: 22611018]

Biographies

Xiaotong Zhang received his B.S. and Ph.D. degrees in Electrical Engineering from Zhejiang University, China, in 2004 and 2009, respectively. He worked as a Postdoctoral Associate from 2009–2012 in Dr. Bin He's lab in Department of Biomedical Engineering (BME) at University of Minnesota (UMN), USA, and then has been working as a Research Associate in UMN BME until now. His research interests cover numerical electromagnetic modeling and computation, electrical properties tomography (EPT) of biological tissues using MRI scanner, quantitative real-time local SAR estimation and management in ultra-high field MRI application, RF magnetic fields mapping (B1-mapping) in MRI, and RF safety in parallel transmission.

Jiaen Liu received his B.S. and M.S. degrees in Engineering from Tsinghua University, Beijing, China, in 2005 and 2007, respectively. He is now a Ph.D. candidate in the Department of Biomedical Engineering at University of Minnesota, Minneapolis, US. Currently, he is working on developing reconstruction algorithms and experiment techniques for MR-based electrical properties tomography and investigating its application in pathology diagnosis and MRI safety. His research interests include functional biomedical imaging, bioinstrumentation, applied mathematics, and computational approaches to understand biological systems.

Bin He (F'04) is Distinguished McKnight University Professor of Biomedical Engineering, Medtronic-Bakken Endowed Chair for Engineering in Medicine, Director of Institute for Engineering in Medicine, Founding Director of Center for Neuroengineering, and Director

of NSF IGERT Training Program in Systems Neuroengineering at the University of Minnesota. Dr. He's research interests cover a broad spectrum in biomedical engineering and neuroscience, including neuroengineering, biomedical imaging, and medical devices. He has made pioneering contributions to functional neuroimaging, brain-computer interface, cardiac electrophysiological tomography, and bioimpedance imaging. He has published over 200 peer reviewed articles in leading international journals and delivered over 300 plenary, keynote, and invited talks and seminars in international conferences and institutions worldwide. Dr. He was a recipient of the NSF CAREER Award, the AHA Established Investigator Award, and the Outstanding Research Award from the International Federation of Clinical Neurophysiology. He is a Fellow of IEEE, AIMBE, International Academy of Medical and Biological Engineering, and Institute of Physics.

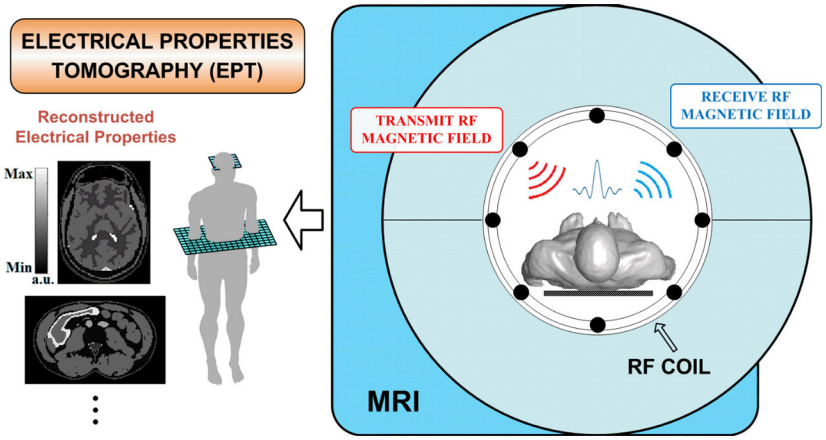

Figure 1.
Conceptual diagram of Electrical Properties Tomography.

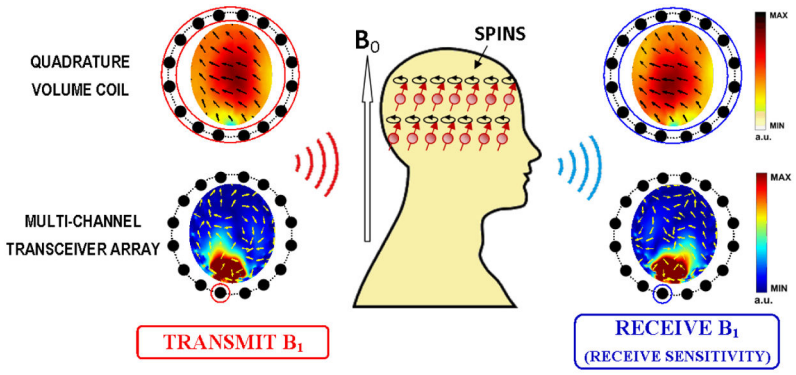

Figure 2.

B1 field components on a transverse plane, when using a quadrature volume coil (3T; upper row) and a multi-channel transceiver array (7T; bottom row) for head imaging. In the transceiver array, a single coil element is used for RF power transmission and signal reception. Color maps indicate the magnitude of complex B1 fields, while arrows represent their phase variations in space (real part in horizontal direction vs. imaginary part in longitudinal direction).

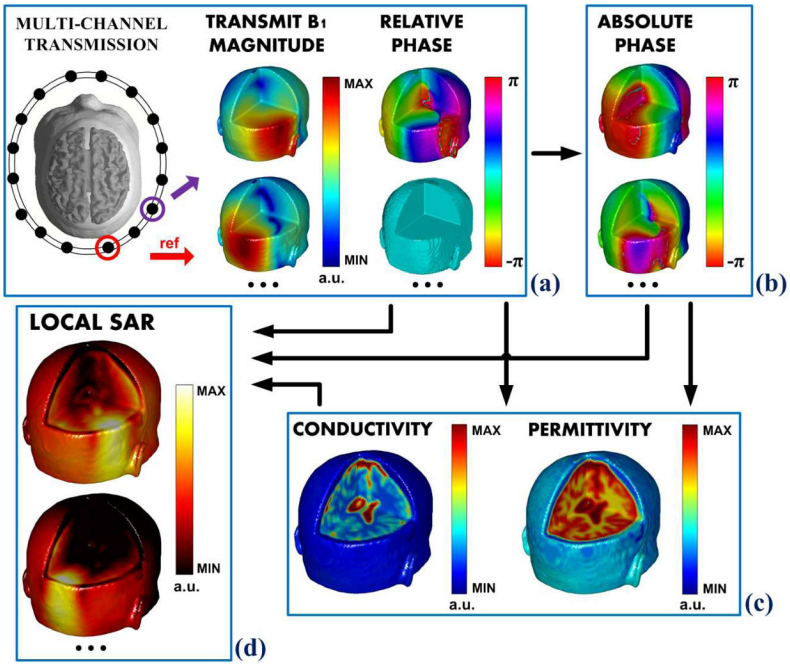

Figure 3.

A flowchart of EPT problem when using a multi-channel transceiver array. Taking a reference channel, (a) the magnitude and relative phase distributions can be measured for each coil element, then (b) their absolute phase can be computed, and (c) the electrical properties can be reconstructed. Ultimately, utilizing all measurable and retrieved information, (d) local SAR for each coil element can be estimated.

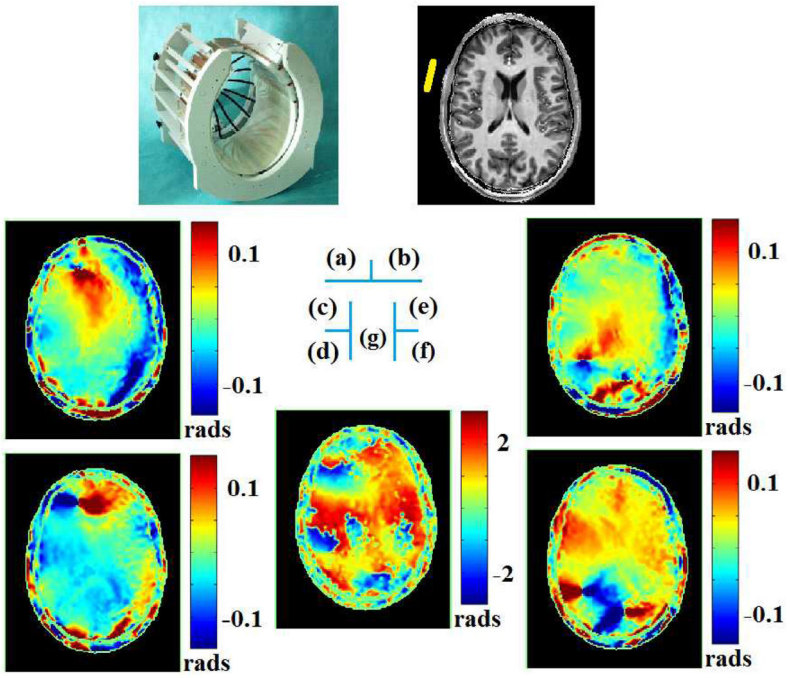

Figure 4.

When using a 16-channel transceiver array (a) for brain imaging, on a human subject, for a selected reference coil element and on the slice of interest (b), computed x- (c) and y- (d) gradients of transmit B1 phase, (e) x- and (f) y-gradients of receive B1 phase, and (g) phase difference between transmit and receive B_1 [49],[50].

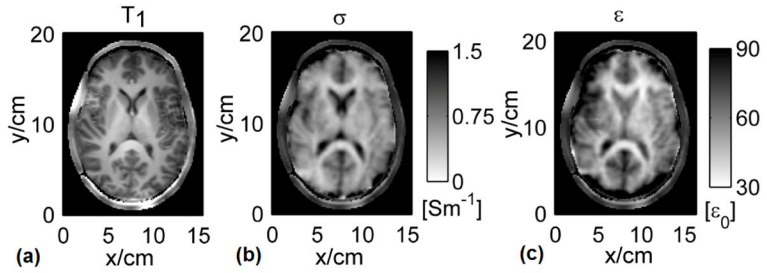

Figure 5.

Human results on a transverse slice: (a) the normalized T1-weighted images, (b) reconstructed conductivity and (c) relative permittivity images [75].

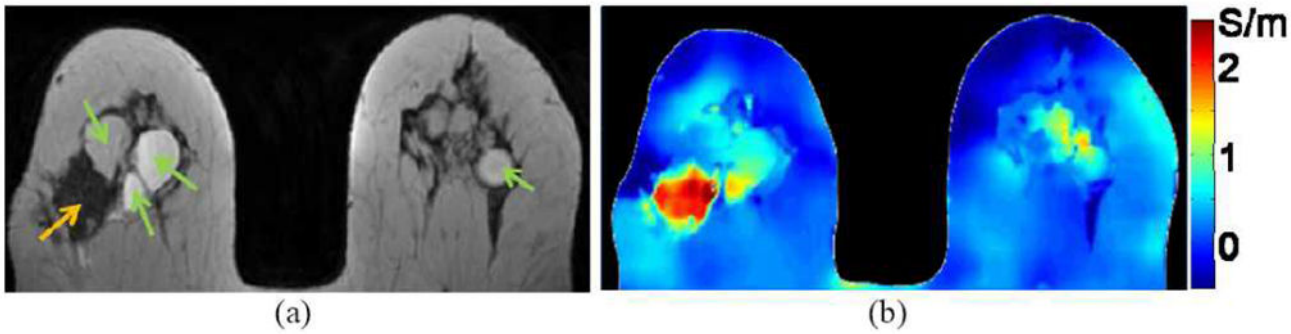

Figure 6.

Breast cancer imaging example. (a) TSE image, showing several cysts (green arrows) and tumor (orange arrow). (b) Conductivity of breast shown in (a). Low/medium/high conductivity is found for fat/cysts/tumor, respectively. (From [76] with permission)

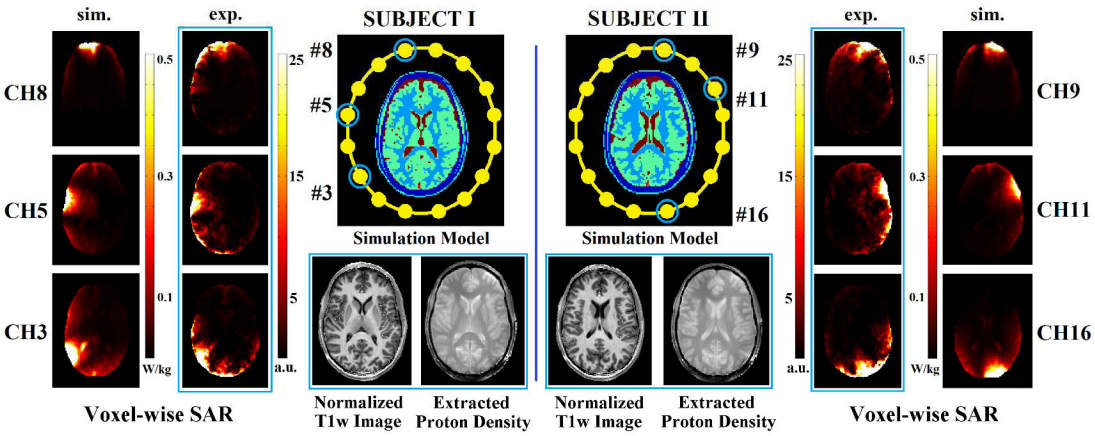

Figure 7.

Using a 16-channel transceiver head coil, on two human subjects, normalized T1w images, extracted proton density, and estimated voxel-wise local SAR for selected channels. Simulation results on slices (with similar anatomical structures) shown as references. (Experiment results encircled by blue rectangles) (From [91] with permission)